Applications of Dissipative Particle Dynamics

Robert D. Groot

Unilever Research & Development, Olivier van Noortlaan 120, 3133 AT Vlaardingen,
The Netherlands

Abstract. Dissipative Particle Dynamics (DPD) is one of the most promising simulation techniques for studies of mesoscopic properties of soft matter systems. Here, we discuss DPD, its parameterisation in simple systems, as well as in polymeric systems using the Flory–Huggins theory, and generalisations of DPD. Block copolymer mesophase separation, polymers and membranes in surfactant solutions, and biomembrane morphology and rupture will shown as specific examples.

1 Why Mesoscopic Simulation?

Over the last two decades most simulation studies have concentrated on the motion of individual atoms in systems of a few nanometers and a few nanoseconds. Other simulation methods concentrate exclusively on the macroscopic world of planes, trains and automobiles. However, between the nano- and macroscopic scale ranges some forty decades in volume and time. The holy grail of theoretical physics is to bridge this gap. This is due to the fact that in many cases simulation of this intermediate regime is essential for understanding macroscopic phenomena, e.g. molecules ordering spontaneously on mesoscopic length and time scales. This category of problems includes life and biological phenomena such as membrane structuring, perforation and trafficking. As a matter of fact, this list contains all soft condensed matter including surfactants, polymers and (multi)block copolymers that show microphase separation, or form gels or glassy systems, see Fig. 1.

What could we expect if we would be able to extend the time scale over which we can simulate a physical system? If we take the example of lipid bilayers, we find that new phenomena occur every time we increase the time scale at which we look at our system [1]. On the shortest time scale of a few picoseconds the lipids show bond and angle fluctuations of dihedral angles within the same molecule. On larger time scales of a few tens of picoseconds, trans-gauche isomerizations of dihedrals occur [2]. On a time scale of a few nanoseconds the phospholipids rotate around their axis, and on the time-scale of tens of nanoseconds two lipids switch place within a bilayer, giving rise to lateral diffusion. Within this time scale the individual lipids orient, and lipid membranes show protrusions [3]. Finally, on a time-scale of 100 ns peristaltic motions and undulations occur [4].

By virtue of parallelization over several processors or PC clusters, hardware developments have now pushed the limit of molecular simulations to 100 ns [4]. Nevertheless, there is a limit beyond which hardware developments cannot help us. For instance, phenomena such as co-operative motion in phase transitions, insertion of large molecules

R.D. Groot, Applications of Dissipative Particle Dynamics, Lect. Notes Phys. **640**, 5–38 (2004)
http://www.springerlink.com/

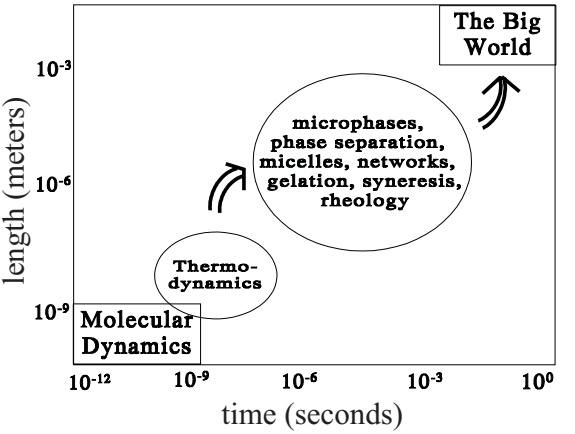

Fig. 1. The mesoscale gap. Time is given in seconds

like proteins into membranes, or membrane fusion occur on much larger time scales and are well outside the range of current simulation power. This requires simulation of the microsecond range, while a new set of phenomena could be studied if we could address the millisecond time scale.

The question thus arises how these phenomena can be modelled. One approach is the dissipative particle dynamics method (DPD). Here, a number of atoms are grouped together into one simulation bead which is used as the new simulation element. The reliability of the result obviously depends on how the underlying atoms translate into the interaction parameters between the DPD beads. Some semi-empirical methods will be discussed here. Then we concentrate on three applications: The mesophase formation of block copolymers, the simulation of polymer-surfactant complexes in bulk solution and the interaction of biological membranes with surfactant.

2 Introduction to DPD

The strategy to simulate molecular motions on length- and time scales that are much larger than what can be achieved with ordinary Molecular Dynamics simulations is based on two main ingredients. First, atoms are lumped together into "united atoms" describing more than one atom. The second ingredient used is that these new particles interact with each other via rather soft forces as the positions of the underlying atoms are smeared out. As we want to describe the correct thermodynamics (and dynamics) on a larger length-scale than an atom, we only need to reproduce the correct compressibility of the liquid and the correct solubilities of the various components into each other [5]. To arrive at this goal, we have the freedom to choose the effective interaction as a rather soft repulsion, provided that we satisfy the criteria discussed above. This means that we can leave out the hard core repulsive interaction between the atoms. Since it is the hard core interaction that forces the use of small time-steps (10^{-15} s), the removal of this core allows a considerable increase of the time-step, typically four orders of magnitude.

2.1 Forces

In DPD a set of interacting particles, whose time evolution is governed by Newton's equation of motion, is considered. Hence, at every time-step the set of positions and velocities, $\{\mathbf{r}_i, \mathbf{v}_i\}$ follows from the positions and velocities at earlier time. The force acting on a particle is given by the sum of a conservative, drag and pair-wise additive random force, i.e. $f_i = \sum_j (F_{ij}^{\mathrm{C}} + F_{ij}^{\mathrm{D}} + F_{ij}^{\mathrm{R}})$ where the sum runs over all neighbouring particles within a certain distance R_{c}. All forces depend on coordinate differences. The conservative force is given by

$$F_{ij}^{\mathrm{C}} = \begin{cases} -a_{ij}\left(1 - |\mathbf{r}_{ij}|/R_{\mathrm{c}}\right)\hat{\mathbf{r}}_{ij} & \text{if } |\mathbf{r}_{ij}| < R_{\mathrm{c}} \\ 0 & \text{if } |\mathbf{r}_{ij}| > R_{\mathrm{c}} \end{cases},$$

where a_{ij} is a maximum repulsion between particle i and particle j, $\mathbf{r}_{ij} = \mathbf{r}_j - \mathbf{r}_i$ and $\hat{\mathbf{r}}_{ij} = \mathbf{r}_{ij}/|\mathbf{r}_{ij}|$ [5,6], see Fig. 2.

Between neighbouring particles on a chain an extra spring force is defined to bind the particles together,

$$F_{ij}^{\mathrm{S}} = 4\mathbf{r}_{ij} \qquad \text{if } i \text{ is connected to } j.$$

The drag force F_{ij}^{D} and the random force F_{ij}^{R} act as heat sink and source, respectively, so that their combined effect is a thermostat. The random force is given by

$$F_{ij}^{\mathrm{R}} = \sigma\omega\left(r_{ij}\right)\hat{\mathbf{r}}_{ij}\zeta/\sqrt{\delta t}$$

and the drag force as

$$F_{ij}^{\mathrm{D}} = -\frac{1}{2}\sigma^2\omega\left(r_{ij}\right)^2/k_{\mathrm{B}}T\hat{\mathbf{r}}_{ij}\left(\mathbf{v}_{ij}\cdot\hat{\mathbf{r}}_{ij}\right),$$

where ζ is a random variable with zero mean and unit variance, and $\omega(r) = (1-r)$ for $r < 1$ and $\omega = 0$ for $r > 1$.

The amplitude of the random force should be taken proportional to $1/\sqrt{\delta t}$. Why is this? Let $\theta(t)$ be the random force exerted on a particle at a particular time step. This force leads to Brownian motion, where the displacement of a particle is proportional to

$$R \sim \sqrt{N_{\mathrm{steps}}}\delta r = \sqrt{\frac{1}{\delta t}}\theta\delta t \sim \sqrt{t} \times \theta\sqrt{\delta t}.$$

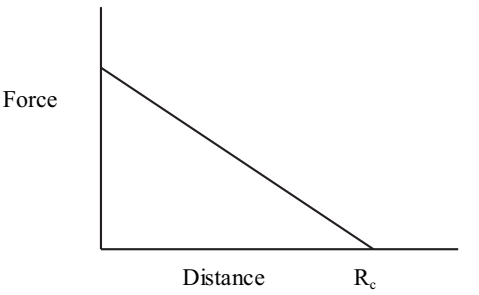

Fig. 2. The conservative force used in DPD

Since the displacement should not depend on the particular time step that we have chosen to simulate the process, $\theta(t)$ should be proportional to $1\sqrt{\delta t}$. This particular thermostat is special in that it conserves (angular) momentum leading to a correct description of hydrodynamics [7]. The reason why this thermostat conserves hydrodynamics is quite profound. All forces acting on particles are exerted on them by other particles nearby. This holds for the conservative forces, as well as for the friction and random forces. Since all particles obey Newton's third law, the sum of all forces in the system vanishes. Moreover, if we take any given volume of liquid, then all forces exerted between particles enclosed by that volume vanish. Consequently, the total acceleration of this volume of liquid equals the sum of all forces that cross the boundary of the volume. This is the very condition that leads to the Navier–Stokes equation. Therefore, whatever interaction force we invent between the particles, as long as it is a local interaction and satisfies Newton's third law we will always have hydrodynamics. If the random force would not be implemented pair-wise, but instead relative to a fixed background, we would break Newton's law. This is the case in Brownian Dynamics. Momentum is no longer conserved, and no hydrodynamic interaction is present in the simulation.

We choose the particle mass, temperature and the interaction range as units of mass, energy and length, hence $m = k_{\mathrm{B}}T = R_{\mathrm{c}} = 1$ and the simulated time is expressed in the natural unit of time

$$\tau = R_{\mathrm{c}}\sqrt{\frac{m}{k_{\mathrm{B}}T}}.$$

The DPD method in general has been shown to produce a correct (N,V,T) ensemble if the fluctuation-dissipation relation is satisfied [5,8]. Why is this important? In general the state of the system can be represented by a vector in 6N-dimensional space, $\{\mathrm{r}^{3\mathrm{N}}, \mathrm{p}^{3\mathrm{N}}\}$. The probability to find the system at any point in phase-space is the density of states $\varrho\{\mathrm{r}^{3\mathrm{N}}, \mathrm{p}^{3\mathrm{N}}\}$. The evolution of the system in phase-space can formally be written via the Liouville equation, which is

$$\frac{\partial \varrho}{\partial t} = \mathcal{L}\varrho = \mathcal{L}_{\mathrm{d}}\varrho + \mathcal{L}_{\mathrm{c}}\varrho. \tag{1}$$

In this equation $\mathcal{L}$ is the Liouville operator, which we can split to operators related to the conservative ($\mathcal{L}_{\mathrm{c}}$) and the dissipative force ($\mathcal{L}_{\mathrm{d}}$). If we turn off all noise and friction in the simulation the latter vanishes, and the evolution is solely governed by $\mathcal{L}_{\mathrm{c}}$. In equilibrium, the density of states does not change, and hence $\mathcal{L}_{\mathrm{c}}\varrho_{\mathrm{eq}}$ must be zero. Here ϱ_{eq} is the Boltzmann distribution:

$$\varrho_{\mathrm{eq}} \propto \exp\left(-\frac{U\left(r^{3\mathrm{N}}\right)}{k_{\mathrm{B}}T} - \sum_i \frac{p_i^2}{2m_i k_{\mathrm{B}}T}\right).$$

If we now check (1), it is clear that the dissipative Liouville operator acting on the Boltzmann distribution must also vanish, otherwise the equilibrium would shift to another distribution when noise and friction are turned on. To maintain the correct Boltzmann distribution, noise and friction must therefore be administered in a particular way. Español and Warren [8] proved that if we choose any distance dependent noise term

$$F_{ij}^{\mathrm{R}} = \sigma\omega(r_{ij})\hat{\mathbf{r}}_{ij}\zeta/\sqrt{\delta t},$$

then the friction term must be taken as

$$F_{ij}^{\mathrm{D}} = -\frac{1}{2}\sigma^2\omega(r_{ij})^2/k_{\mathrm{B}}T\hat{\mathbf{r}}_{ij}\left(\mathbf{v}_{ij}\cdot\hat{\mathbf{r}}_{ij}\right).$$

2.2 Simulation Techniques

At every time-step the set of positions and velocities, $\{\mathbf{r}_i, \mathbf{v}_i\}$, is updated from the positions and velocities at earlier time. All update algorithms known from Molecular Dynamics can be used in principle [9], but the presence of the velocity in the forces complicates things. A straightforward method is to use the Euler scheme

$$\begin{aligned}
\mathbf{r}_i\left(t+\delta t\right) &= \mathbf{r}_i(t) + \mathbf{v}_i(t)\delta t,\\
\mathbf{v}_i\left(t+\delta t\right) &= \mathbf{v}_i(t) + \mathbf{F}_i(t)\delta t,\\
\mathbf{F}_i\left(t+\delta t\right) &= f\left(\mathbf{r}_i(t+\delta t), \mathbf{v}_i(t+\delta t)\right).
\end{aligned}$$

However, temperature control is not very accurate in this method. To use a second order update algorithm is not as straightforward as it may seem. A second order algorithm integrates the positions from t to $t+\delta t$ using the velocity and accelerations known at t. To update the velocities, however, we need to know the accelerations at time t and at time $t+\delta t$. In ordinary Molecular Dynamics this is not a problem since the forces at time $t+\delta t$ are known once the new particle positions are calculated. In DPD, however, we need to know the velocity in the next time step in order to calculate the force that we need to update the velocities.

Two solutions to this problem are worth mentioning. The first is a modified version of the velocity-Verlet algorithm [5]:

$$\begin{aligned}
r_i(t+\delta t) &= r_i(t) + \delta t\, v_i(t) + \frac{1}{2}\delta t^2 f_i(t),\\
\tilde{v}_i(t+\lambda\,\delta t) &= \tilde{v}_i(t) + \lambda\delta t\, f_i(t),\\
f_i(t+\delta t) &= f_i\left(r_i(t+\delta t), \tilde{v}_i(t+\lambda\,\delta t)\right),\\
v_i(t+\delta t) &= v_i(t) + \frac{1}{2}\delta t\left(f_i(t) + f_i(t+\delta t)\right).
\end{aligned} \tag{2}$$

The masses of the particles are set to 1, so that the force acting on a particle equals its acceleration. The force is updated once per iteration. The velocity in the next time-step is estimated by a predictor method. This is done in the second step of our algorithm. The velocity is corrected in the last step. If the parameter λ is put at $\lambda = 0.5$ this scheme equals the velocity-Verlet algorithm [10]. It is empirically observed that if we use $\lambda = 0.65$ we find a very accurate temperature control, even at the time-step $\delta t = 0.06\tau$. This is probably due to a cancellation of errors. A more systematic study into the influence of parameter λ was presented by Den Otter and Clarke [11].

The second method, presented by Pagonabarraga et al. [12] can be seen as an extension of this algorithm. In this method the same update scheme as in (2) is used, but the velocity dependent part of the force is iterated until a stable value for the velocity in the new time step is obtained. The scheme is therefore named self-consistent. Because it is self-consistent, the simulation algorithm is also time-reversible. This is found to have an important influence on the temperature control. For most practical applications, however, the predictor method is comparably accurate, but faster.

2.3 Parameterisation

This has two parts, the first is to derive the correct length- and time scales of the simulation, and the second is to obtain the repulsion parameters. DPD can be used either as a flow solver or as a method to simulate molecular dynamics over time scales far beyond what can be reached with Molecular Dynamics. If it is used as a flow solver, the time scale of the simulation is related to hydrodynamic relaxation time of the problem. This must be matched between the simulation and the problem. In practice, this calibration is done by adjusting the viscosity of the fluid. If explicit molecules and their diffusive behaviour are simulated, we need to match, e.g. the diffusion coefficient of water. Here we concentrate on the latter application of DPD. Since water is an important compound we will use it to define the length- and time scales used in 'molecular' DPD [13].

Let a bead correspond to $N_{\rm m}$ water molecules. The number $N_{\rm m}$ can be viewed upon as a real-space renormalization factor. Thus, a cube of volume $R_{\rm c}^3$ represents $\varrho N_{\rm m}$ water molecules, where ϱ is the number of DPD beads per cubic $R_{\rm c}$. From the density of water and its molecular weight, we can calculate the volume per water molecule in liquid water at room temperature as $30\,\mathring{\rm A}^3$. Thus, the physical volume of this cube equals $30\,\varrho N_{\rm m}\mathring{\rm A}^3$, hence the length scale $R_{\rm c}$ follows as

$$R_{\rm c} = 3.107(\varrho N_{\rm m})^{1/3}\ (\mathring{\rm A}).$$

To gauge the unit of time, we match the long-time diffusion coefficient of water. Some care must be taken here. The self-diffusion coefficient of a water bead is not the same as the self-diffusion coefficient of water, since the bead represents $N_{\rm m}$ water molecules. When these move over the vectors $\mathbf{R}_1, \mathbf{R}_2, \ldots \mathbf{R}_{N_{\rm m}}$, their centre of mass moves over the vector $\mathbf{R}_{\rm w} = \left(\mathbf{R}_1 + \mathbf{R}_2 + \ldots + \mathbf{R}_{\rm N_m}\right)/N_{\rm m}$. Hence the ensemble average of the mean square displacement of the water beads is

$$R_{\rm w}^2 = \langle \mathbf{R}_{\rm w} \cdot \mathbf{R}_{\rm w} \rangle = \frac{\left(\langle \mathbf{R}_1 \cdot \mathbf{R}_1 \rangle + \langle \mathbf{R}_2 \cdot \mathbf{R}_2 \rangle + \ldots\right)}{N_{\rm m}^2} = \frac{R^2}{N_{\rm m}},$$

where R^2 is the mean square displacement of a water molecule. At the noise and repulsion parameters $\sigma = 3$ and $a = 78$, the diffusion coefficient of water beads in DPD simulation was obtained as

$$D_{\rm w} = 0.1707(14)R_{\rm c}^2/\tau.$$

Equating this to the experimental diffusion coefficient of water [14] $D_{\rm water} = (2.43 \pm 0.01)\times 10^{-5}\,{\rm cm}^2/{\rm s}$, leads to the time scale

$$\tau = \frac{N_{\rm m} D_{\rm sim} R_{\rm c}^2}{D_{\rm water}} = 14.1 \pm 0.1 N_{\rm m}^{5/3} \quad ({\rm ps}). \tag{3}$$

In this equation it is implicitly assumed that the repulsion parameter between equal beads is fixed to the value $a = 78$, and that the bead density is fixed at $\varrho = 3$.

At this point we can understand why the DPD method is so much faster than straightforward molecular dynamics. There are two combined effects that lead to speed-up. The first contribution comes from the low Schmidt number in the simulation [5]. The Schmidt

number is the ratio between viscosity and the self-diffusion coefficient, $Sc = \nu/D$. In an ordinary liquid like water, this ratio is roughly $Sc \approx 1000$, whereas in the DPD method we have $Sc \approx 1$. The origin of this difference can be traced back to the removal of the hard core from the interaction potential. This hard core leads to a caging effect, i.e. an atom undergoes many collisions before it is actually transported. The soft potential used here removes this caging affect, so that the mobility of particles is increased by a factor of 1000. The second factor contributing to the speed-up is the scaling of the physical time with the renormalization factor N_m as in (3). On top of the power 5/3 by which the physical time scale increases, the amount of CPU time will decrease inversely proportional to N_m if we want to simulate a given volume, simply because we have to update the position of fewer objects. Thus, for a given system volume, DPD can be expected to be faster than MD by a factor of roughly $1000\, N_\mathrm{m}^{8/3} \approx 2{\times}10^4$ for $N_\mathrm{m} = 3$ and about 10^5 for $N_\mathrm{m} = 6$. This is independent of hardware and disregards the CPU time spent on evaluating the (relatively long ranged) Lennard-Jones potential.

To find the interaction parameters for this model, we need to match the liquid structure function in the limit $k \to 0$, as this determines the free energy change associated to density fluctuations. This in turn is related to the compressibility and solubilities. Note that the pressure itself drops out in an NVT ensemble, as this is a linear variation of the free energy. It was previously proposed that the following relation should hold [5]:

$$\frac{1}{k_\mathrm{B}T}\left(\frac{\partial p}{\partial \varrho}\right)_\mathrm{simulation} = \frac{1}{k_\mathrm{B}T}\left(\frac{\partial p}{\partial n}\right)_\mathrm{experiment},$$

where ϱ is the bead density in the simulation, and n is the density of e.g. water molecules in liquid water. However, this relation only holds if one DPD bead corresponds to one water molecule. In general, the system should satisfy

$$\frac{1}{k_\mathrm{B}T}\left(\frac{\partial p}{\partial \varrho}\right)_\mathrm{simulation} = \frac{1}{k_\mathrm{B}T}\left(\frac{\partial n}{\partial \varrho}\right)\cdot\left(\frac{\partial p}{\partial n}\right)_\mathrm{experiment} = \frac{N_\mathrm{m}}{k_\mathrm{B}T}\left(\frac{\partial p}{\partial n}\right)_\mathrm{experiment},$$

where N_m is the number of water molecules per DPD bead. When N_m is chosen as $N_\mathrm{m} = 3$, the compressibility of water at room temperature is matched if the repulsion parameter between particles of the same type is determined at $a_{ii} = 78$. Note that it is taken the same for all liquid components, as we actually simulate equal liquid volumes for all components.

The next parameters to determine are the bead-bead repulsions, by matching solubility. In polymer chemistry solubility is usually expressed by specifying the Flory–Huggins χ-parameters. This parameter represents the excess free energy of mixing in the Flory–Huggins model. This is a cell model, where every cell is filled by a fraction ϕ of A molecules and by a fraction $1-\phi$ of B molecules, i.e. the lattice is completely filled. If A is a polymer occupying N_A cells, and B is solvent that occupying N_B cells, the free energy per cell (disregarding constants and terms linear in ϕ) can be written as

$$\frac{f_\nu}{k_\mathrm{B}T} = \frac{\phi\ln\phi}{N_\mathrm{A}} + \frac{(1-\phi)\ln(1-\phi)}{N_\mathrm{B}} + \chi\phi(1-\phi).$$

Different polymers usually tend to segregate, see Fig. 3. To model this behaviour we impose a larger repulsion between unlike beads than between beads of the same type.

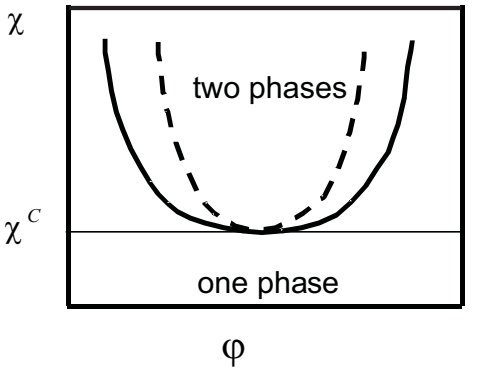

Fig. 3. The demixing curve (*full curve*) and spinodal (*dashed curve*) in Flory–Huggins theory

It has been established that the χ-parameter is linearly related to the *excess* of the AB repulsion over the AA repulsion [5]. When the volume fraction of A in the majority B phase is measured for two liquids, each consisting of molecules of length N, the χ-parameter can be obtained by substituting the simulated volume fraction into the mean-field expression for the binodal:

$$\chi N = \frac{\ln(1-\phi) - \ln\phi}{1-2\phi}. \tag{4}$$

This expression should be valid far away from the critical point. For $a_{ii} = 78$ this led to the correspondence [13]

$$\chi N = 0.231 \pm 0.001 \Delta a,$$

where $\Delta a = a_{\mathrm{AB}} - a_{\mathrm{AA}}$ is the excess repulsion.

The pertinent χ-parameters can be determined by matching the Flory–Huggins model to relevant experimental solubility data. An alternative to the use of mean-field theory as an intermediate was provided by Wijmans et al. [15]. They simulated the binodal in a mixture of a polymer and a single bead solvent using the Gibbs ensemble Monte Carlo method. This led to the binodal curve:

$$\Delta a \approx 0.516 N^{-0.751} \left| N^{0.435} \ln(1-\phi) - \ln(\phi) \right|^{1.826} + 2.25\left(1 + N^{-0.44}\right)^{1.75},$$

where N is the number of beads per polymer. This equation enables us to compare simulations to experiments directly, or alternatively to extract the simulation parameters from experimental data.

2.4 Generalisations and Alternatives

DPD, as described above, is like a minimal version to simulate a molecular liquid. For particular applications, particles can and indeed have been given internal degrees of freedom, such as an internal energy [16,17], angular momentum and orientation [18]. The former generalisation allows constant energy simulations, so that heat flows can

be simulated. The latter generalisation describes particles with spin, leading to higher viscosity. Another variation is to use each particle as a centre for a weighted density functional [19]. This gives the freedom to insert any desired free energy functional, and thus alter the equation of state, and simulate free surfaces.

DPD is by no means the only technique by which mesoscale simulations can be performed. One option is to use Lagrangian flow solvers. By adapting this approach a simulation technique for modelling viscoelastic fluid flow has been developed by Yuan, Ball and Edwards [20]. By using a moving Voronoi mesh, the method is able to track the details of fluid behaviour, e.g. deformation and stream lines in viscoelastic liquids. The velocity (and pressure, etc.) is defined on discrete points, which are convected with the flow. The points exchange momentum with their neighbour, and the interactions are chosen by discretising the Navier–Stokes equations.

Smoothed Particle Hydrodynamics (SPH) is a similar scheme without a mesh. It uses an interpolation scheme to calculate spatial derivatives based on weight functions centred around the particles. The particles interact via a pairwise interaction, and pressure is included explicitly. Newton's 3rd law is not obeyed, but the scheme is close to that of DPD [21].

Chris Lowe introduced a variation of DPD [22] in which the interaction potential is the same, but the velocities of the particles are exchanged rapidly via an Andersen Monte Carlo method [23]. New relative velocities are taken from a Maxwell distribution, so that the temperature control is rigorous. When small steps are taken and the velocities are exchanged at every step, this method leads to much higher viscosity than DPD. In fact, any Schmidt number can be chosen. On the other hand, low viscosity is problematic.

Another alternative is the Lattice Boltzmann method, which is used to solve the Navier–Stokes equations on a lattice. The lattice is chosen as a 3D projection of a 4D fcc lattice. This choice minimises lattice artefacts. On this lattice a discrete implementation of the Boltzmann equation is simulated. When a fluid mixture is to be simulated the same lattice may serve as a basis for a Landau expansion of the free energy [24]. Thus, the method contains no explicit molecules, and no noise is needed. Finally self-consistent field theory can also be used to simulate diffusive problems of, e.g. block copolymers on a 3D lattice [25]. Here a lattice is used to calculate the polymer Green functions. From the Green functions follow the local polymer volume fractions. These in turn determine the local chemical potentials of the various segments. The chemical potential gradients are coupled to the polymer mobility via Onsager kinetic coefficients. This leads to a Smoluchowski equation for the density fields which can be solved numerically. Because the polymer statistics is by construction Gaussian, this method is strictly speaking not valid for polymer solutions. Experiments indicate that also block copolymers have markedly non-Gaussian statistics even quite close to their critical point.

All methods mentioned here have positive and negative properties, this also holds for DPD. The unresolved issues in DPD are as follows. First, the Schmidt number problem. The speed by which momentum diffuses is the kinematic viscosity ν, the speed by which particles travel is the diffusion coefficient D. The Schmidt number is $Sc = \nu/D \sim 1000$ in a liquid like water, whereas it is of the order 1 in DPD. This effectively means that the diffusion coefficient is overestimated by a factor of 1000 when the viscous time scale is matched. When viscous flow is to be simulated correctly, an alternative to classical DPD

is the Andersen Monte Carlo method by Lowe. For molecular processes that are diffusion controlled, however, fast diffusion is a great help to speed up the simulation. The second problem appears when the method is used for turbulent hydrodynamic problems. The rather soft beads lead to a low sound velocity. This means that at high Reynolds numbers, one may run into unwanted supersonic flow. To repair this flaw, the incompressibility of the liquid has to be built into the method by other means than by soft repulsive particles. Finally, when long polymers and micelles are to be simulated, or breaking oil droplets in a surfactant solution, one may run into a clash of length scales. To resolve a coarse-graining where individual surfactant molecules are simulated (1 nm resolution), and to simulate micron size droplets at the same time (1 μm size) requires a simulation of order 10^{10} particles. This is presently not possible in DPD, but this problem is generic for all mesoscale methods.

Although DPD is a rather new technique it has already been applied to a wide variety of problems including complex two-phase flow, such as the rheology of dense colloidal suspensions [26], the break-up of oil droplets in gravitational and shear fields [27], and spinodal decomposition and domain growth [28–30]. In the next two sections we concentrate on a small number of applications, the phase formation of block copolymers, polymer-surfactant interactions and the simulation of biomembranes.

3 Block Copolymer Mesophase Separation

3.1 Polymers in Melt

Diblock copolymers are polymers consisting of two linear blocks (A and B) of mutually insoluble polymers, chemically connected end-to-end. When a melt of these polymers is quenched (i.e. the temperature is suddenly dropped), the A-blocks and B-blocks tend to phase separate. The connectivity of the polymers prevents macroscopic phase separation, and, consequently, the system can only reduce its free energy by connecting the A-rich and B-rich domains in structures like spheres, rods, sheets, perforated sheets or complicated sponge-like structures. This principle has been known for quite some time, see Bates and Fredrickson for a review [31], but only in recent years our understanding as to which phase is formed under what conditions has increased to a level where we are in the position to predict the phase diagram. The question as to which structure is formed under what condition was first theoretically studied by Leibler [32], who used Gaussian coil statistics to calculate the free energy in a Landau theory. The equilibrium microstructure in this theory depends on the ratio f of the length of the A section relative to the total length of the polymer, and on the mutual solubility of the A and B units, which is usually represented by the Flory–Huggins χ-parameter [31]. We want of a theory, or a simulation method, to be able to resolve the following issues:

1. To predict the phase structure of diblock copolymers as function of f, χ and M_{n}.
2. To understand the dynamics of formation of a phase after a temperature quench.
3. To describe the transition of a copolymer system from one mesophase structure into another.

Since the driving force for the formation of mesophases comes from the surface tension between phases A and B, this needs to be reproduced correctly. Also the conformation and dynamics of homopolymers in the melt needs to be correct. For homopolymers

the theory predicts that the endpoint separation as function of polymer length N in a melt should scale as

$$R_{\mathrm{e}} \sim N^{1/2}.$$

Furthermore, the diffusion coefficient and the relaxation time of the end-to-end vector should scale as [33]

$$D \sim N^{-1} \text{ and } \tau_R \sim N^2.$$

Spenley has checked these scaling relations [34]. He found that

$$R_{\mathrm{e}} \sim (N-1)^{0.498\pm0.005}\ ,\ D \sim N^{-1.02\pm0.02}\ ,\ \text{and } \tau_R \sim N^{1.98\pm0.03}.$$

The correspondences are excellent. For the surface tension of an ordinary liquid near its critical point one may expect the scaling law [35]

$$\sigma \sim (1 - T/T_{\mathrm{c}})^{\mu},$$

where T_{c} is the critical temperature, and μ is an exponent that takes on the value $\mu = 1.26$ for the Ising model, and $\mu = 3/2$ for the van der Waals liquid. Groot and Warren have simulated the surface tension between two homopolymer melts in the DPD model [5]. They noted that for a polymer-polymer interface, T corresponds to $1/\chi$ and that the critical χ-parameter between two homopolymers is $\chi_{\mathrm{c}} = 2/N$, and thus found the following master equation for the surface tension:

$$\sigma/R_{\mathrm{c}} = 0.58\,\varrho kT\chi^{0.4}(1 - 2/\chi N)^{3/2}.$$

The power 3/2 is expected, as one often finds mean-field theory to work well for polymers. The prefactor $\chi^{0.4}$ is at variance with mean-field theory, which predicts a factor $\chi^{1/2}$. The polymer length dependence of the surface tension appears to match quantitatively with experimental results, see Fig. 4.

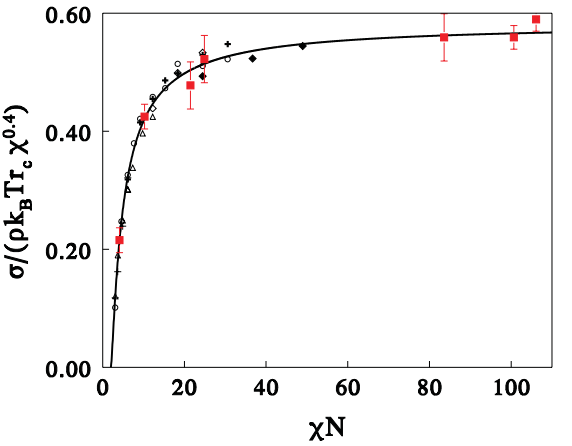

Fig. 4. Simulated polymer-polymer surface tension master curve and experimental data, reproduced from [5,36]

3.2 Expected and Simulated Phase Diagram

To the lowest order, mean-field theory predicts that the block copolymer phase diagram is determined only by product χN, and by the ratio $f =$ (length of A block) divided by the total length of polymer, see Fig. 5. Therefore, to lowest order we can rescale a long polymer down to a small number of segments per chain. DPD simulations of block copolymers were performed by Groot et al [36,38], who used a polymer length $N = 10$ and $\chi N \approx 46$. This is well outside the weak segregation limit. Configurations of A_5B_5 and A_3B_7 polymer systems containing 40 000 particles are shown at time $\tau = 4\,000\tau \cong 430\tau_R$, where τ_R is the Rouse time of a homopolymer of the same molecular weight. Due to symmetry of the polymer the A_5B_5 system must be either lamellar (for large χN) or disordered (for small χN), but when the A:B ratio is changed away from 1:1 other phases are experimentally found to appear [31]. In the simulation it is indeed found that the A_5B_5 system converges to a lamellar phase, see Fig. 6. The A_3B_7 system, in contrast, does not converge to a lamellar phase. The A-domains are shown as white spots in Fig. 6.

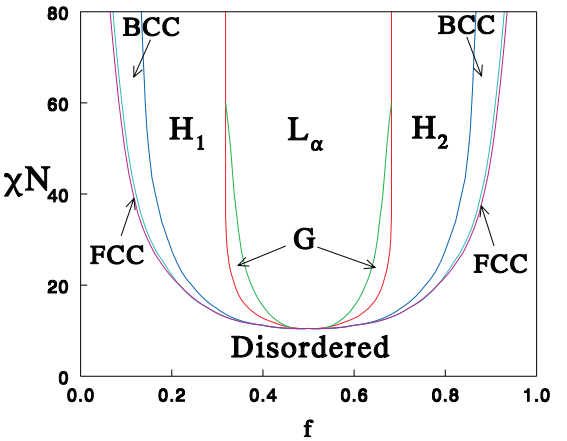

Fig. 5. Expected phase diagram based on work by Matsen and Bates [37] and reproduced from Groot and Madden [36]

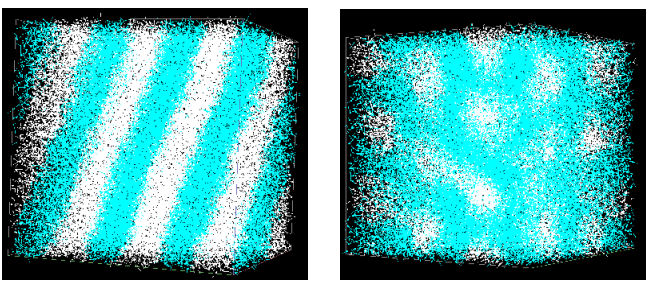

Fig. 6. Conformation of A_5B_5 system (left) and A_3B_7 system (right), after [36]

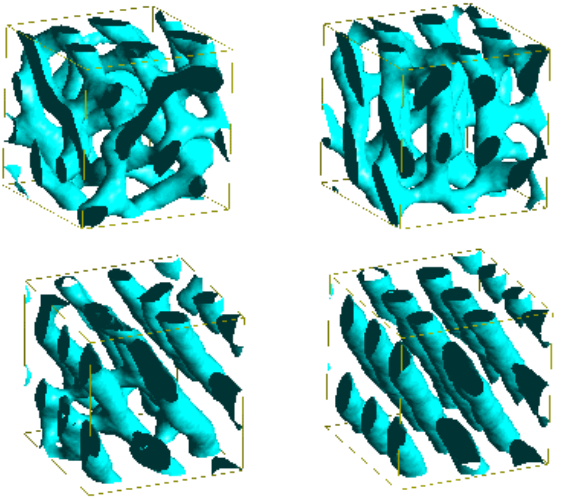

Fig. 7. Evolution of A_3B_7 block copolymer system, after [36]

The time evolution of the A_3B_7 system is shown in Fig. 7. In the top left conformation we see a structure that resembles the gyroid phase, but which is predicted to be unstable. After a further 2 000 time units we find the top right structure. Note that the system of rods has lost symmetry relative to the earlier stage, i.e. the rods tend to align in a co-operative manner. In the next stage, shown in the bottom left picture of Fig. 7, the rods are completely aligned, though some sideward connections are still present. In the final configuration the sideward connections are broken and the system is locked in a state of parallel rods in a perfectly hexagonal arrangement. These results show that the DPD method is capable of changing the topology of a micro-phase structure in an efficient way. Qualitatively, it is found that the A_5B_5 system evolves to the lamellar phase as it should, and that the A_3B_7 system evolves to a hexagonal phase, which is expected to be stable between $0.165 < f < 0.314$ for the present χ-parameter.

In a subsequent study simulations were performed on a range of polymeric systems: A_5B_5 ($f = 0.5$), A_4B_6, ($f = 0.4$), A_3B_7 ($f = 0.3$) and A_2B_8 ($f = 0.2$) and A_1B_9 ($f = 0.1$). The latter remained an isotropic liquid throughout the course of the simulation. Apart from the A_2B_8 system, all of the simulations finally produce a phase structure that is consistent with self-consistent field theory. To further quantify the phase diagram near the H_1-Lα phase transition line, simulations of mixed polymers were done. Assuming that for these mixtures the mean value of f is representative of a homopolymer system of the same value of f, A_3B_7 and A_4B_6 polymers were mixed to create systems of *average* value $\langle f \rangle = 0.325$, 0.35 and 0.375. In experiments, Zhao et al. [39] also blended two block-copolymers to obtain a mixture with a preferred (mean) asymmetry, $\langle f \rangle$. These experiments indicate that the mixture behaves as a homopolymer as long as the difference between the two polymers is small. In simulations, all systems within the predicted lamellar phase region did indeed converge to a lamellar phase, and the same holds for the hexagonal phase region. However, between the hexagonal phase and the lamellar phase DPD does not produce a gyroid phase but a perforated lamellar phase

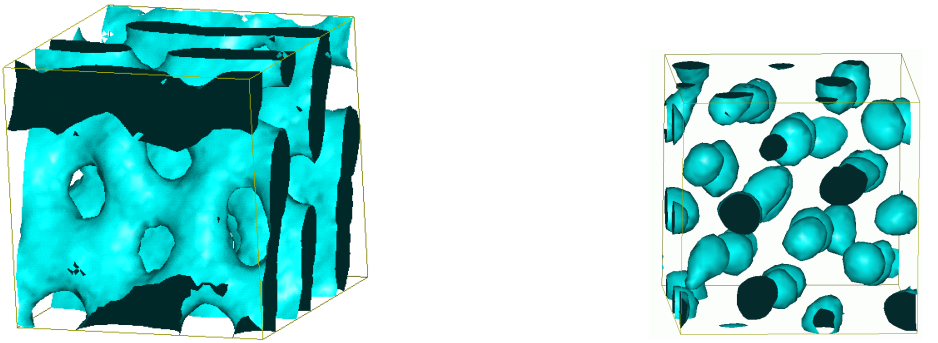

a) **b)**

Fig. 8. **a)** Perforated lamellar system for $\langle f \rangle = 0.35$, after [36]. **b)** Body-centred cubic system at $\langle f \rangle = 0.14$, after [36]

instead, see Fig. 8. This phase has recently been identified in experiments [39,40], but it has not been predicted from self-consistent field theory.

For the A_2B_8 system theory predicts a hexagonal phase. In the simulation this system forms a disordered micellar phase that lasts the total length of the simulation, 32 000 time units. To proceed, polymers of structures A_2B_8 and A_3B_7 were blended. Of these the system with $\langle f \rangle = 0.275$ evolved to the hexagonal phase, and the systems with $\langle f \rangle \leq 0.25$ remained in a liquid-like, entangled tube state during the course of the simulations. Hence at $\chi N = 46$ simulation predicts a phase transition from an entangled tube state to a hexagonal phase near $f_c \approx 0.26 \pm 0.02$. At this point we note that at low f we do not find the expected BCC quasi-crystalline phase, but instead we find a liquid-like ordering in flexible micelles. To understand the differences between theory and simulation, we need to study the influence of the finite chain length.

The simulated polymers are only of length $N = 10$. This increases artificially the importance of fluctuations relative to really long polymers. Thus fluctuations lower the free energy of isolated micelles relative to that of infinitely long rods. For surface tension the finite polymer length is apparantely not very important, but for the phase diagram the effects due to finite length can be severe. Weak coupling calculations predict that the order-disorder transition at $f = 0.5$ for small polymers shifts up as [41]

$$(\chi N)_c = 10.5 + 41.0\bar{N}^{-1/3}.$$

For simulations with small polymer lengths this would imply that the effective χ-parameter (i.e. corresponding to infinite N) is smaller by a factor

$$(\chi N)_{\text{eff}} = \frac{10.5}{10.5 + 41.0\bar{N}^{-1/3}}\chi N = \frac{\chi N}{1 + 3.9\bar{N}^{-1/3}}. \tag{5}$$

The decrease of the effective χ-parameter is controlled by fluctuations characterised by a Ginzburg parameter

$$\bar{N} = 6^3(R_g^3\varrho_p)^2 = (R_e^3\varrho_p)^2,$$

where $\varrho_{\rm p}$ is the polymer concentration and $R_{\rm g}$ the radius of gyration [31]. It is this $\bar{N}$ which appears at the right hand side of (5). This parameter is determined by the number of other polymers in the volume that a polymer occupies. Substituting the end-point separation that we obtained for homopolymers, and polymer density $\varrho_{\rm p} = \varrho/N$ we find

$$(\chi N)_{\rm eff} = \frac{\chi N}{1 + 4.3\varrho^{-2/3}N^{-1/3}} \approx 0.51\chi N$$

for our simulations at $N = 10$. The effective χ-parameters would thus be given by $(\chi N)_{\rm eff} = 23.4$. From the simulations we find a reasonable match with mean-field theory at $(\chi N)_{\rm eff} = 20 \pm 2$, though the location of the H-G transition is slightly off.

The consequence of this is that these simulations should be compared with the theoretical phase diagram at $\chi N \approx 20$. If this assertion is correct we should find a BCC phase for the $f = 0.14$ system when we considerably increase χN over the value that we currently used, as this would put us in the middle of the cubic phase. Therefore, a number of runs at various values for f and χ were performed so as to follow the theoretically predicted BCC phase boundary. Intermediate values of f were obtained by blending A_1B_9 with A_2B_8. The structure at $f = 0.14$ and $\chi N = 98$ is shown in Fig. 8b. This system rapidly forms spherical micelles, which afterwards form a quasi-crystalline phase on a much larger time-scale.

If we compare the theory to the simulation results at $\chi N = 20$, we actually find a matching correspondence. Theory predict the transitions from disordered-FCC, FCC-BCC, BCC-hexagonal, hexagonal-gyroid and gyroid-lamellar at f = 0.210, 0.214, 0.240, 0.340 and 0.374. The DPD results for the equilibrium structure of block-copolymers are in line with this, and are summarised in the schematic phase diagram shown in Fig. 9. The "effective" Flory–Huggins parameter is obtained by extrapolation to infinitely long chains using finite chain simulations. This diagram is based on 27 systems and should only be seen as a rough indication of which phase we find where. The diagram compares well to the diagram that Larson produced for short lattice chains in a monomer solvent [42]. In accordance with mean-field theory the simulated diagram shows the classical quasi-solid body centred cubic (BCC), hexagonal (H), and lamellar phases (L). However, we also find melted structures like a liquid micellar phase (LM), a liquid rod

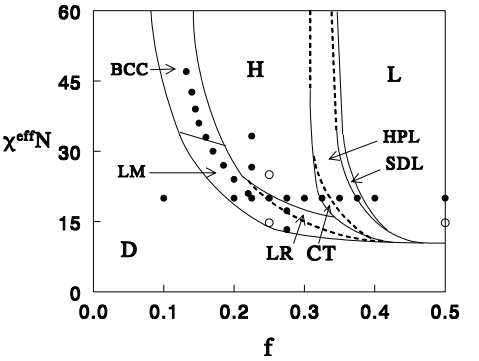

Fig. 9. Rough phase diagram coming forward from DPD simulations, after [38,44]

phase (LR) and a connected tube phase (CT). These melted structures agree with experimental observation [43] and with Monte Carlo simulations of block copolymers. The DPD simulations also predict a hexagonally perforated lamellar phase (HPL) which has been observed in experiments [39,40], and a small region where screw dislocations in a lamellar phase are stabilised (SDL).

3.3 Evolution Pathways

An important advantage of the DPD method is its explicit results for time-dependence. This is very relevant for polymer microphase separation, since for long polymers the typical evolution time can be long, especially when the polymers are branched. For grafted polymers, the time that a side-branch needs to disjoin from one micelle sets a natural scale for the time of topological rearrangements. If a polymer melt is quenched from a high temperature into the ordered phase, the pathway through which the final structure is reached is relevant if the time of interest is months rather than minutes or hours. To introduce the formation process of the mesophases we briefly repeat the qualitative findings from DPD simulations that have been reported elsewhere [36,38,44]. Processes on three different length- and time- scales can be distinguished by the formation of polymer micro-phases:

1. phase separation on the mesoscopic bead level,
2. organisation of polymers into micelles,
3. organisation of micelles into a superstructure with its own particular symmetry.

A schematic diagram summarising the different effects is shown in Fig. 10. The evidence for this scheme comes from observing the time evolution of polymer systems of various compositions at a fixed value of χN, and capturing the qualitative effects

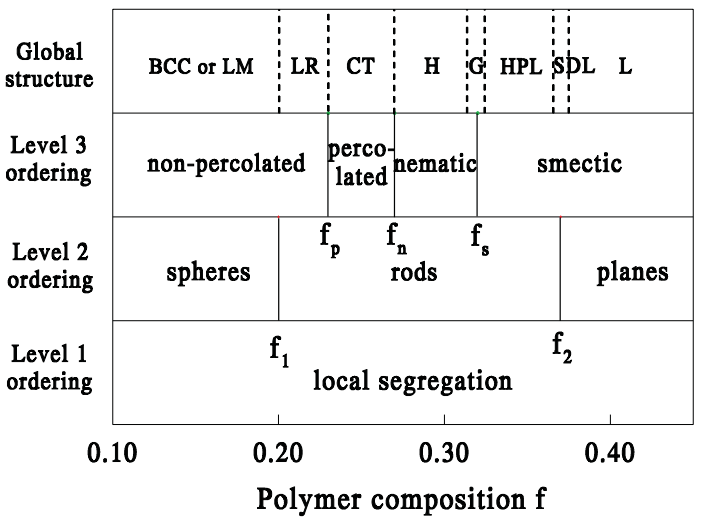

Fig. 10. Schematic diagram of evolutionary processes, after [38,44]

of the evolution in a simple picture. This is a conceptual framework, which helps to rationalise the evolution, rather than an exact description of the location of various transition points. These obviously depend on the precise value of χN. Effects on different length-scales interplay in both the final structure and in the pathway to form it. On level 2, the dimensionality of the micelles (spherical, rod-like or planar) is the dominating factor. At the AB segregation parameters used in these simulations, the transitions between these structures are found at $f_1 \approx 0.20$ and $f_2 \approx 0.37$. On a global level (level 3) the important transition points are the percolation transition, where the rods form a interconnected tube network, the nematic transition and the smectic transition. These are located respectively at $f_{\rm p} \approx 0.23$, $f_{\rm n} \approx 0.27$ and $f_{\rm s} \approx 0.32$. For compositions where $f_{\rm p} < f < f_2$ a percolating interconnected tube phase is formed as precursor of the final phase. Experimental evidence comes from time-resolved X-ray scattering, see Balsara et al. [45] and references therein. These experiments reveal the presence of two processes, a fast process that is believed to be related to the local segregation of the blocks (ordering levels 1 and 2) and a slow process that leads to long-ranged order (level 3).

3.4 Importance of Hydrodynamics

A clear comparison to establish the role of hydrodynamics can be made when simulations are performed with and without hydrodynamics. Two continuum simulation methods have therefore been compared. Both describe the same Hamiltonian system, but they differ in their evolution algorithm. The first method is the Dissipative Particle Dynamics method, and the second is the Brownian Dynamics method. The only difference between the two is that all hydrodynamic interactions are taken into account in the former method, but not in the latter. The polymer architecture, connectivity, interactions and the liquid compressibility are explicit in both methods. Thus we can make a very pure comparison, to see what happens if only hydrodynamics is turned off while all other physical effects are included. For symmetric polymers the soft sphere model is found to predict the formation of lamellar domains of some eight lamellae across, irrespective of the presence of hydrodynamic interactions. Without external shear experimental samples remain globally disordered, but local order does appear spontaneously. Experimental systems also form domains of some eight lamellae across, hence they order on the length-scale seen in the DPD simulations.

Since different compositions lead to aggregates of different topology, it is not clear beforehand if the influence of hydrodynamic interactions is equally important in the different regions of the phase diagram. For this reason we have performed simulations both for asymmetric polymers ($f = 0.3$), and for symmetric polymers ($f = 0.5$). In the former the system has to go through a percolated state and a nematic transition to find its equilibrium structure and in the latter system domains of local lamellar order have to grow together to form a macroscopically homogeneous phase. We first discuss the results obtained for the A_3B_7 copolymer system. The simulations were performed in a box of $V = 20{\times}20{\times}20$ using periodic boundary conditions. At time $t = 0$, 2400 copolymers of structure A_3B_7 were arranged randomly in the box and the systems were allowed to evolve.

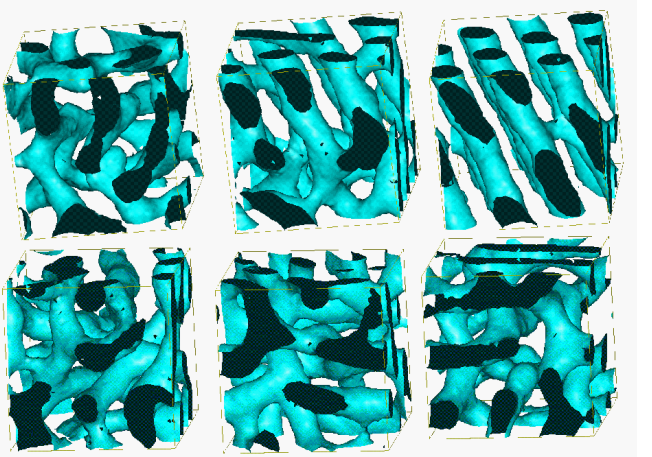

Fig. 11. Evolution of A_3B_7 system with hydrodynamics (DPD, top row) and without hydrodynamic interaction (Brownian Dynamics, bottom row), after [36]

Figure 11 shows three stages in the evolution of the simulated system. The DPD simulation quickly forms micro-phase separated regions that percolate into interconnected tubes. These tubes form a globally disordered fluid phase with tubes changing shape and moving relative to each other. After approximately $7\,500\tau$ a domain of hexagonal order is formed, which grows at the expense of the disordered phase. The subsequently formed hexagonal phase is stable for the rest of the simulation. On the basis of self-consistent field calculations it has recently been put forward [46] that the hexagonal phase is formed from the gyroid by a process where first five-fold connection points are formed, that subsequently break into a three-fold connection and two unconnected tubes. We did not find evidence for this mechanism in our simulations. Instead, we find only three- and four-fold connection points linked by short liquid bridges that sever by a necking mechanism. In the last stages of evolution, where the sample is almost completely hexagonally ordered, we find local defects in the form of liquid bridges between otherwise parallel rods. The dominant mechanism for topological transitions in that stage is the scission of these liquid bridges, see the top-right picture in Fig. 11.

The path taken by the Brownian Dynamics (BD) simulation is very similar to that of the of the DPD simulation in its early stages: the formation of a phase of interconnected tubes. In the BD simulation we also find the tubes to align locally in a hexagonal structure, but this phase is subsequently destroyed again. In many places throughout the simulation box small hexagonal domains arise and disappear. None of these domains manage to grow out to a globally ordered hexagonal phase, even when the simulation is extended to $24\,000\tau$. One may argue that there could be a subtle bug in the BD program, which makes the hexagonal phase unstable [47]. If that would be the case then it is obvious that the hexagonal phase does not form in the BD simulation. To check this loophole, the hexagonal structure, as generated by the DPD simulation, was used as a starting configuration and was evolved in a BD simulation over 50 000 time steps ($3\,000\tau$). The hexagonal phase remained stable. In fact the shape fluctuations of the tubes are smaller

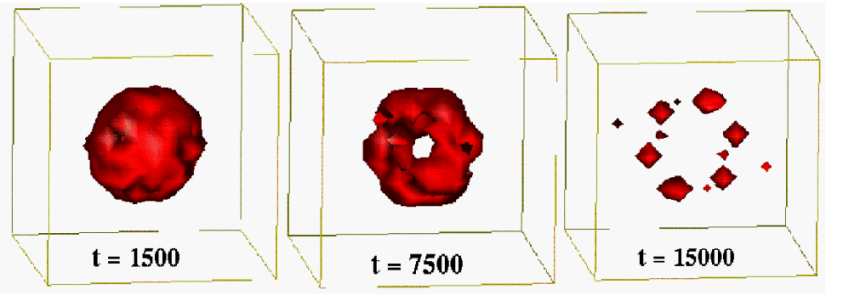

Fig. 12. Evolution of A_3B_7 structure function in DPD, after [36]

than they are in the DPD simulation. So either the hexagonal phase is metastable, but the BD method cannot break it apart, or it is stable and the BD method cannot form it. In either case it is demonstrated that there is a kinetic barrier that the BD method cannot cross. Since the DPD method can cross this barrier, and since the only difference between the two simulation methods is the conservation of momentum leading to a correct description of hydrodynamics in the DPD method, we conclude that hydrodynamic interactions are important in order to cross this barrier.

To define an order parameter for the structure we calculate the structure function:

$$S(\mathbf{k}) = \varrho_{\mathrm{A}}(\mathbf{k})\varrho_{\mathrm{A}}(-\mathbf{k})/N_{\mathrm{A}},$$

where N_{A} is the number of A-particles in the simulation. Its time evolution for the DPD system is shown in Fig. 12. What we observe is that the system in Fourier-space first peaks in a spherical shell around the origin (left). This already corresponds to level 2 ordering (see Fig. 10) as the real-space structure (top-left in Fig. 11) is an isotropic network of tubes; level 1 ordering takes place on a much shorter time-scale. When level 3 ordering sets in ($t \approx 7\,500\tau$) the spherical symmetry is broken, and a ring structure emerges. In real-space this ring corresponds to a hexagonal domain embedded in a network of tubes, see top-middle structure in Fig. 11. This ring subsequently breaks in two halves, that thereupon each break up in three peaks, Fig. 12 middle and right.

The time dependence of the structure function demonstrates that the ordering mechanism goes through various stages, where fewer and fewer modes contribute to the structure. It is this decreasing number of modes contributing to $S(k)$ that is characteristic for the increasing amount of order. Therefore we would like to count the number of k-vectors that contribute to the structure. Since $S(k)$ can be interpreted as a density of states in Fourier space, we define an order parameter by analogy to the entropy of particles distributed in real space as

$$P = \int S(\mathbf{k}) \ln S(\mathbf{k}) \, \mathrm{d}^3\mathbf{k}.$$

Since this is a non-linear functional of the structure function, it distinguishes between systems having a different number of peaks, but the same overall segregation, i.e. it is a measure of the number of independent modes that contribute to the structure.

In Fig. 13 this order parameter is shown for the DPD simulation (with hydrodynamics) and for the BD simulation (without hydrodynamics). The A_3B_7 simulation results

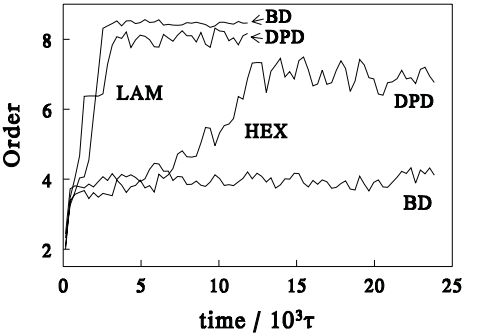

Fig. 13. Evolution of order parameter for A_3B_7 and A_5B_5 systems in DPD and BD, after [36]

are marked HEX. Whereas the DPD simulation shows a continuous increase in order (i.e. self-structuring of the system), the other simulation shows no clear trend. The behaviour of the order parameter demonstrates that hydrodynamic interactions are essential in driving this system to the structure of lowest free energy for this particular point in composition space.

To study the importance of hydrodynamics to the formation of the lamellar phase, a melt of A_5B_5 block copolymers was studied with DPD and BD. As reported previously [36], the DPD simulation swiftly finds its lamellar equilibrium structure. In the light of the previous observations one might expect that the BD simulation does not find the correct equilibrium, because hydrodynamic interactions are absent. However, the BD simulation does converge to the correct equilibrium, following exactly the same dynamics as the DPD system does. Both with and without hydrodynamics the system orders into a single lamellar domain, hence hydrodynamics is not essential for the formation of a lamellar phase. The increase of the order parameter in these simulations is also shown in Fig. 13; the curves are marked LAM. Note that here the time-scale of evolution is much shorter than for asymmetric polymers (marked HEX), where a connected tube structure is formed in the second stage of evolution. The time to form the hexagonal phase is about a factor 8 larger than the time to form the lamellar phase.

For asymmetric copolymers the DPD simulation, which includes hydrodynamics, produces the hexagonal phase predicted by theory and other simulation studies. However, the Brownian Dynamics simulation, which does not include hydrodynamics, does not produce the expected phase but remains trapped in an intermediate structure of interconnected tubes. From these results we conclude that hydrodynamics is important in driving the kinetics of micro-phase separation when an interconnected tube phase is formed as an intermediate structure. This intermediate structure is formed as a precursor for the hexagonal phase and the perforated lamellar phase. Indeed in the formation of the HPL structure [36,44] we found a similar slow evolution as in the formation of the hexagonal phase. The result presented here is a typical example; we have found a very similar pathway and slow evolution in other points within the hexagonal and HPL phases. For symmetric block copolymers that evolve along a pathway that avoids the intermediate connected tube structure, the system evolves quite efficiently if no hydrodynamic interactions are included. Hence hydrodynamic interactions are not critical in this case. The

observed mechanism for micro-phase separation is one of the simultaneous formation of domains of lamellar order throughout the box, whereas the nucleation-and-growth mechanism is pertinent to form the hexagonal phase.

Why is this the case? The nature of the symmetry change between isotropic and hexagonal requires the transition to be of the first order: the Landau expansion contains a non-zero cubic coefficient. This is not the case for the isotropic to lamellar transition, which (in the Landau expansion) is second order, but becomes weakly first order when fluctuations are taken into account [32]. Hence there is a natural tendency for a nucleated process in the former transition, whereas this is not the case in the latter. Therefore, the isotropic to lamellar transition must be spinodal. Nucleation-and-growth can be expected to occur when the disordered phase is *meta-stable*, i.e. when a free energy barrier separates the two phases. Now the hexagonal phase arises from a disordered network of tubes. We speculate that this phase is meta-stable because it resembles the gyroid structure (one might refer to it as a melted gyroid phase), and because of the previous symmetry argument. This implies a (strong) first order transition. Hence the hexagonal phase can be expected to grow via a nucleation-and-growth mechanism. The lamellar phase is formed from a structure of disordered lamellae, which is topologically different from the gyroid phase. There is no stable phase that resembles a disordered lamellar system. Therefore this structure is unstable with respect to the lamellar phase (i.e. the isotropic to lamellar transition is second order or weakly first order), and thus the lamellar phase must form via a spinodal growth law.

4 Polymers and Membranes Interacting with Surfactant Solutions

4.1 Polymers and Surfactants in Solution

The DPD model has first been applied to polymers in solution by Kong et al. [48] and the precise scaling relations were checked by Spenley [34]. These results show that even polymer chains as short as $L = 10$ beads follow the correct endpoint distribution and are characterised by the correct scaling exponents. For a well soluble polymer in solution, theory predicts the endpoint separation and relaxation time to scale as

$$R_\mathrm{e} \sim N^{0.59} \quad \text{and} \quad \tau_R \sim R_\mathrm{e}^3 \sim N^{1.77}.$$

The simulation results by Spenley are [34]

$$R_\mathrm{e} \sim (N-1)^{0.58\pm0.04} \quad \text{and} \quad \tau_R \sim N^{1.80\pm0.04},$$

which is a very good correspondence between theory and simulation.

For the same model the binodal has been simulated by Wijmans et al. [15], using the Gibbs Ensemble Monte Carlo method, see Fig. 14. In these simulations the polymer volume fraction at the critical point scales as

$$\phi_\mathrm{c} \approx \frac{1.53}{2.06 + N^{0.38}} \; ; \; \Delta a_\mathrm{c} \approx 2.25\big(1 + N^{-0.44}\big)^{1.75}.$$

This should be compared to the mean-field Flory–Huggins expressions for the critical volume fraction and the critical χ-parameter as function of the polymer length:

$$\phi_\mathrm{c}^\mathrm{FH} = \frac{1}{1+\sqrt{N}} \quad \text{and} \quad \chi_\mathrm{c}^\mathrm{FH} = \frac{1}{2}\left(1 + \frac{1}{\sqrt{N}}\right)^2.$$

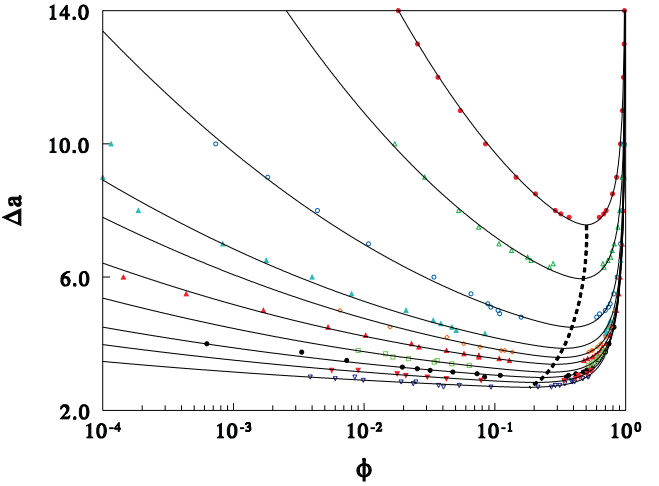

Fig. 14. Binodal curves for soft sphere model, data obtained from Wijmans et al. [15]

Experiments cited by Wijmans et al. indicate a scaling behaviour $\chi_c \sim N^{-0.37}$. Again the correspondence between simulation and experiment is very good, much better than the correspondence between experiment and mean-field theory.

To simulate a surfactant solution with the DPD model Jury et al. [49] used a minimal model. Surfactant was represented by two beads, each representing head (H) and tail (T) parts. When this is dissolved in a solvent (W), we have a model of a symmetric non-ionic surfactant like $C_{12}EO_6$ in solution. The repulsion parameters were fixed at $a_{HH} = a_{TT} = a_{WW} = 25$, $a_{HT} = 30$, $a_{HW} = 0$, and $a_{TW} = 50$. The temperature in the simulation was changed from $k_BT = 0.5$ to $k_BT = 2.5$ and the surfactant concentration from 10 % to 100 %. Very similar phase separation kinetics was observed as in the block copolymer systems described above. They find a micellar phase, a hexagonal phase, a lamellar phase and a disordered structure, in line with the experimental phase diagram of $C_{12}EO_6$. This indicates that the DPD model can indeed be used to study the phase behaviour of complex liquids.

The above results also suggest that DPD is a good candidate to simulate the interaction of polymers with a surfactant solution. The generally accepted picture is that complete micelles adsorb on the polymer [50–52], leading to a necklace of micelle pearls on a polymer backbone [53]. However, small angle neutron scattering (SANS) data on the poly(ethylene oxide) and sodium dodecyl sulfate (SDS) system by Chari et al. [54] suggest that the polymer resembles a swollen cage, rather than a necklace around SDS micelles. Fluorescence measurements on the same system indicate that the aggregation number of SDS is low at the onset of binding, but increases with surfactant concentration where the aggregate forms an elongated rod [55]. For PEO/SDS (PEO = polyethyleneoxide) mixtures it is also found that on increasing SDS concentration the polymer initially reduces in size, but when the surfactant concentration is increased beyond a certain point the polymer swells again [56,57].

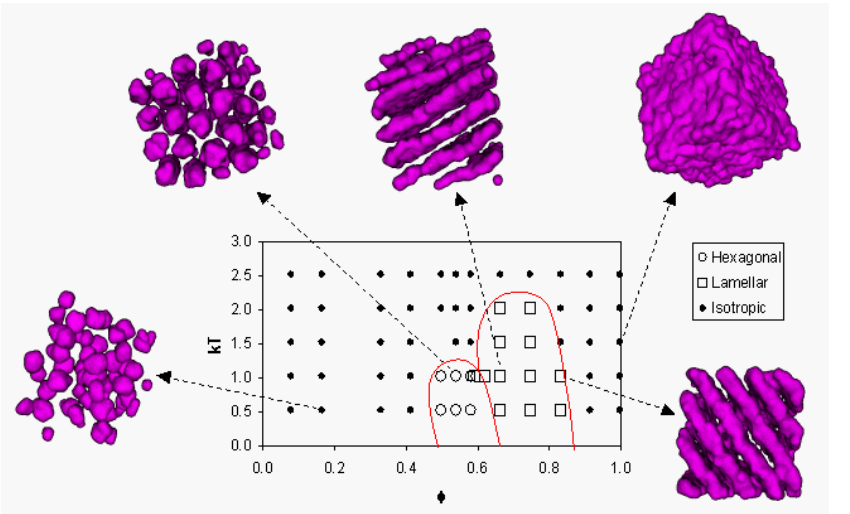

Fig. 15. Phase diagram for minimal surfactant model, after Jury et al. [49]

To predict when in a polymer-surfactant system such molecular bottlebrushes are formed, and when the surfactant adsorbs as micelles, Groot employed the DPD technique [58]. Both the polymer and the surfactant molecules are represented by strings of soft spheres. For this model the chemical potential of surfactant in the presence of polymer can be obtained relatively easy using the Widom insertion method. In the present work a number of examples of polymer-surfactant interactions are described, from which we can deduce when we have micelle binding, and when a continuous binding process is pertinent. To model a two-bead surfactant that readily agglomerates in spherical micelles, the head-head repulsion was increased and the tail-tail repulsion was decreased relative to the water-water repulsion. To model a range of polymer-surfactant interactions, various repulsions between the polymer beads and the surfactant tails and head-groups were studied. When the polymer is attracted towards the surfactant tail, the surfactant can be characterised as hydrophobically interacting, when it is not hydrophobically interacting with the polymer the surfactant can still interact via its head-group.

The simulations comprised of one homopolymer (length $L = 50$) in a box of size $10\times10\times10$, with various amounts of added surfactant. Pictures of typical polymer conformations with 10 surfactant molecules added (less than one micelle) and 100 surfactant molecules added (more than one micelle) are shown in Fig. 16. The conformations shown are at 100 and 300 ns, respectively. In the $N_s = 10$ system (on the left) all surfactant molecules are already adsorbed on the polymer at 70 ns. What is observed in a movie of the $N_s = 100$ simulation is that sometimes individual micelles are discernible and the polymer coils from one micelle to another. This textbook state is alternated with a state where the polymer-surfactant complex forms a sausage where all surfactant molecules run across the polymer backbone collectively in a wave-like motion. This break-up of micelles is related to the strong attractive interaction between the polymer backbone and surfactant tails.

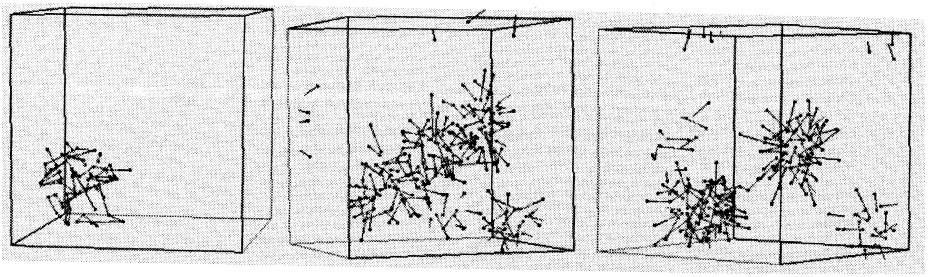

Fig. 16. Polymer-surfactant conformations with 10 surfactant molecules (left) and 100 surfactant molecules (middle and right), after [58]

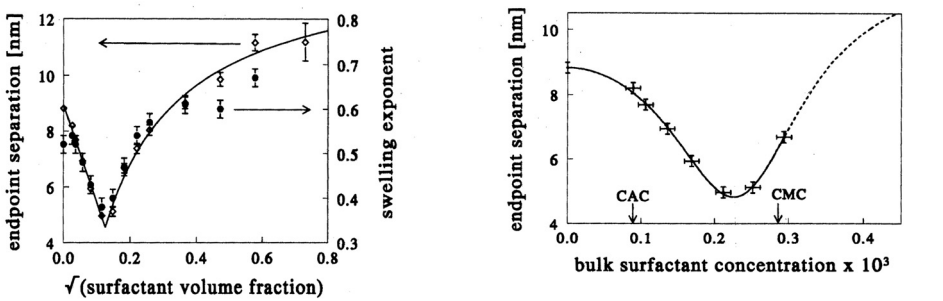

a) **b)**

Fig. 17. **a)** Endpoint separation and swelling exponent passing through minimum, after [58]. **b)** Endpoint separation as function of bulk surfactant concentration, after [58]

Note that in the presence of 10 surfactant molecules the polymer is collapsed, while it is swollen when 100 surfactant molecules are added. All parameter sets studied show the same qualitative behaviour. The polymer endpoint separation is shown in Fig. 17a as a function of the number of surfactant molecules. This figure indicates a dramatic decrease in size of the polymer as the surfactant concentration increases, up to a certain point where precisely one micelle has formed at the polymer. From then on the polymer starts to swell again.

To further analyse the system the endpoint distribution has been fitted to the scaling function [59,60]

$$\ln\left(\Psi(r)\right) = a + \left(\frac{1.026\nu - 0.5}{1-\nu}\right)\ln(r) - br^{1/(1-\nu)},$$

where a and b are arbitrary fit parameters, and ν is the swelling exponent. Upon addition of surfactant the distribution firstly narrows ($N_{\mathrm{s}} = 20$) but for high surfactant concentration the polymer swells again. In Fig. 17a the swelling exponent that is obtained this way is compared with the endpoint separation. The curves are very similar. This plot indicates that an initially marginally soluble ($\nu = 0.5$) polymer undergoes a coil-globule transition ($\nu < 0.4$) when surfactant is added in a particular ratio. When yet more surfactant is added the polymer swells again, even more than a self-avoiding chain, $\nu = 0.65$. This should be contrasted to experimental observations. Chari et al. [54]

obtained the swelling exponent $\nu = 0.65$ for a saturated PEO/SDS system as we find here. Thompson et al. [57] study the thickness of an adsorbed layer of PEO, and find an initial decrease, followed by a subsequent increase when the SDS concentration is increased, very similar to the present simulation results.

In the previous simulations, the number of surfactant molecules in the system was varied. This number takes rather small values, so that in some cases all surfactant molecules are aggregated into the same cluster. What we want is to describe a single polymer in equilibrium with an infinitely large surfactant solution. To determine this equilibrium concentration, the first thing to establish is which quantity determines this equilibrium. For this purpose we study two boxes, one contains polymer, surfactant and water (I), and the other contains only surfactant and water (II).

The total Gibbs free energy of the system comprising the sub-systems I and II is

$$G = \mu_{\mathrm{p}}^{\mathrm{I}} N_{\mathrm{p}}^{\mathrm{I}} + \mu_{\mathrm{s}}^{\mathrm{I}} N_{\mathrm{s}}^{\mathrm{I}} + \mu_{\mathrm{w}}^{\mathrm{I}} N_{\mathrm{w}}^{\mathrm{I}} + \mu_{\mathrm{s}}^{\mathrm{II}} N_{\mathrm{s}}^{\mathrm{II}} + \mu_{\mathrm{w}}^{\mathrm{II}} N_{\mathrm{w}}^{\mathrm{II}},$$

where I and II refer to boxes I and II, and N_{p}, N_{s} and N_{w} are the number of polymer, surfactant and water molecules present in the respective boxes. This thought experiment is an example of the Gibbs ensemble in which the total number of molecules in the two boxes is fixed, but molecules are allowed to move from box I to box II and vice versa. However, as an extra constraint, we impose that the total number of particles in each box is constant. The only allowed moves are swaps of a surfactant molecule from I to II and a simultaneous swap of an equal number of water beads from II to I, and vice versa. The variation of the Gibbs free energy under these swaps is

$$\delta G = \left(\mu_{\mathrm{s}}^{\mathrm{I}} - \mu_{\mathrm{s}}^{\mathrm{II}}\right) \delta N_{\mathrm{s}} - L_{\mathrm{s}} \left(\mu_{\mathrm{w}}^{\mathrm{I}} - \mu_{\mathrm{w}}^{\mathrm{II}}\right) \delta N_{\mathrm{s}},$$

where L_{s} is the number of beads in a surfactant. As in equilibrium $\delta G = 0$, we find

$$\mu_{\mathrm{s}}^{\mathrm{I}} - L_{\mathrm{s}} \mu_{\mathrm{w}}^{\mathrm{I}} = \mu_{\mathrm{s}}^{\mathrm{II}} - L_{\mathrm{s}} \mu_{\mathrm{w}}^{\mathrm{II}} = \mu$$

from which the proper chemical potential follows as

$$\mu = k_{\mathrm{B}} T \ln\left(\varrho_{\mathrm{s}}\right) - L_{\mathrm{s}} k_{\mathrm{B}} T \ln\left(\varrho_{\mathrm{w}}\right) + \Delta\mu_{\mathrm{s}} - L_{\mathrm{s}} \Delta\mu_{\mathrm{w}}.$$

Here ϱ_{s} and ϱ_{w} are the concentrations of surfactant and water molecules respectively. Hence, to calculate the equilibrium concentration of surfactant in a system without polymer we need to measure the excess chemical potentials of both water and surfactant. The bulk surfactant concentration in equilibrium with the polymer-surfactant complex has the same chemical potential. Combining this with the polymer endpoint separation results, we find the curve shown in Fig. 17b.

For hydrophobically interacting surfactants, the chemical potential is a continuously rising function for $0 < N_{\mathrm{s}} < 50$, see Fig. 18a. This behaviour is characteristic for continuous adsorption. In the simulation we find *bottlebrush* conformations at the higher surfactant concentrations. When the head-group repulsion is changed from a net repulsion into a net attraction, the chemical potential curve shifts down, but still has the same initial slope at small surfactant concentration.

However, when the interaction of the polymer with the tail is switched to be repulsive (χ_{pt} is increased from -1.5 to $+2.0$) a dramatic change is observed: the chemical

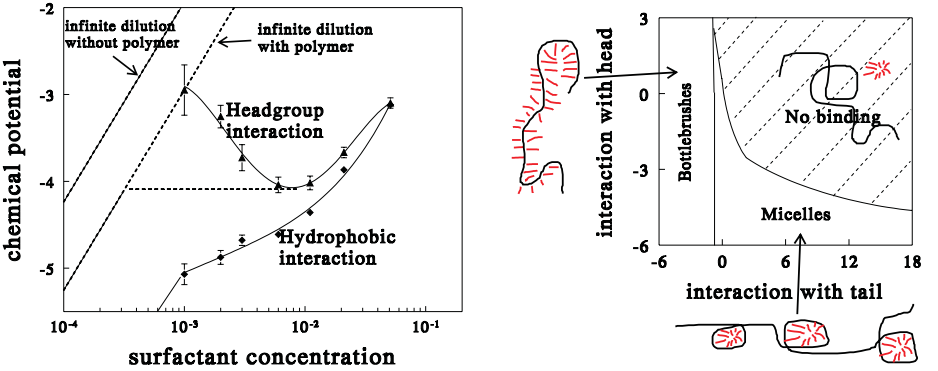

Fig. 18. **a)** Surfactant chemical potential for headgroup/hydrophobic interaction, after [58]. **b)** "Phase diagram" of polymer-surfactant aggregation, after [58]

potential first decreases with surfactant concentration, passes through a minimum, and then increases again. This behaviour signals *micelle adsorption*. When the surfactant concentration in the bulk is slowly increased, the adsorbed amount will follow the infinite dilution limit in the presence of polymer, up to the point where on average 0.3 molecules are adsorbed. Here the chemical potential equals the minimum chemical potential at which adsorbed micelles can exist. At this point the adsorbed amount jumps up to the value corresponding to one adsorbed micelle, see Fig. 18a. Such behaviour is predicted to occur when a strong interaction between surfactant head-group and polymer is pertinent, for instance for the binding of a cationic surfactant to an anionic polymer. This result also implies that when the total surfactant concentration is continuously increased in a system with many polymers present, the bulk surfactant concentration will remain constant at the value corresponding to the critical aggregation concentration (CAC), until a micelle is adsorbed on every polymer in the system. At the CAC, the system contains a mixture of polymers without any surfactant molecules adsorbed, and polymers with a complete micelle adsorbed. These micelles are smaller than the micelles that are formed in the bulk.

To roughly map out when each of the binding modes is pertinent, a number of short runs has been performed throughout the $(\chi_{\rm pt}, \chi_{\rm ph})$ parameter space, for one polymer and 30 surfactant molecules. The result is shown in the "phase-diagram" in Fig. 18b. This diagram should be considered as a qualitative picture, capturing the relevant physical phenomena. To predict such a diagram for a particular surfactant requires a careful tuning of the parameters that have been kept fixed here, viz. the head-group/head-group and the head-group/tail interactions. The qualitative agreement between the available experimental data and the presently studied dumbbell surfactant model warrants a further study to map chemically specific surfactant systems onto the dumbbell model.

4.2 Biomembrane Morphology

Another area in which the DPD method has been applied successfully is the interaction of surfactant with biomembranes. Non-ionic surfactants have traditionally been considered

as mild. However, alcohol ethoxylates are shown to be capable of inhibiting bacterial growth [61]. There is evidence that non-ionic surfactant can interact with *in vitro* lipid membranes by the formation of channels through the membrane [62]. The occurrence of "hole" formation in bilayers of long chain surfactants has been demonstrated for certain non-ionic surfactants by small angle x-ray scattering studies [63]. Similar structures have been found in experiments on block co-polymers [39,40] and in simulations thereof (see Fig. 7). Finally, addition of cationic surfactants to lipid membranes leads to hole formation [64,65]. It therefore seems reasonable to enquire whether the interaction of alcohol ethoxylates and phospholipids typical of bacterial membranes would naturally lead to such mesh phase which would make the bacterial cell leaky and leading to bacterial stasis and ultimately to cell death. No evidence has been found for a structured perforated phase in deuterium NMR and x-ray diffraction studies on the interaction of a phosphatidylethanolamine extract of *Escherichia coli* with an alcohol ethoxylate formulation. For this reason a simulation study was undertaken, to find evidence of moving or temporary holes. Since hole formation and disappearance is expected to occur beyond the time scale that can be reached with molecular dynamics, the DPD simulation method was employed by Groot and Rabone [13].

In the simulated system, three carbon atoms are taken together into one bead. The Flory–Huggins theory was used to derive the relevant χ-parameters from experimental solubilities. To reproduce the correct solubility of hexane, heptane and octane in water, they found $\chi_{\mathrm{hydrocarbon-water}} \approx 6.0$, which appears to be relatively independent of temperature. The second χ-parameter to match that is that between polyethyleneoxide and water. The problem here is that PEO and water at room temperature mix in all ratios, hence the solubility does not lead to a parameter value. At elevated temperatures ($T > 100^\circ$ C), water and PEO no longer mix ideally. Hence an alternative route is to describe this demixing at higher temperatures, and to extrapolate the temperature dependence of the χ-parameter back to room temperature. This way Barneveld et al. [66] estimated this χ-parameter as function of temperature and found the value $\chi_{\mathrm{ew}} \approx 0.30 - 0.38$ at room temperature. However, he only took the cloud-point into account where mean-field theory is least reliable. Taking the shape of the whole binodal into account and extrapolating back to room temperature, Groot and Rabone [13] find from the experimental data by Seaki et al. [67]: $\chi_{\mathrm{ew}} \approx 0.30 \pm 0.04$, which is close to the value obtained by Barneveld.

A third important χ-parameter is the interaction between PEO and hydrocarbons. What experimentally is available is neutron scattering data of $C_{12}E_6$ at the air-water interface [68]. Assuming that this is not too dissimilar from the oil-water interface, this data can be compared to DPD simulation data of an oil-surfactant-water system. The experiment shows a significant overlap between the surfactant head group and the surfactant tails. To arrive at the same amount of overlap in simulation as in the experiment, a χ-parameter much smaller than the hydrocarbon-water parameter needs to be used. A good agreement between the width and overlap of the head and tail peaks as seen in experiment and simulation is found at χ-parameter between hydrocarbons and EO beads $\chi_{\mathrm{ce}} = 2.0$.

Finally the χ-parameters describing the head-group of the lipid molecule were defined. Since these groups contain more oxygen than EO does, and also have partial charges, it has been treated as if it were water, with respect to C and EO. The result-

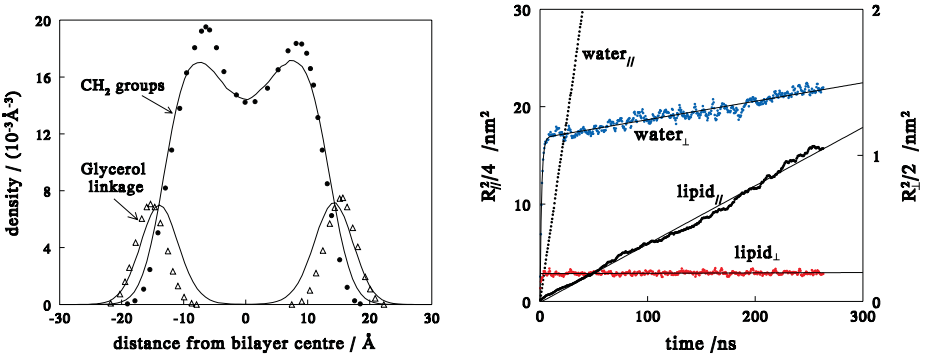

Fig. 19. **a)** DPD bilayer density profile compared to MD density profile, **b)** Displacement of a water and lipid parallel and perpendicular to membrane, after [13]

ing bilayers have been compared with molecular dynamic simulations of 1-palmitoyl-2-oleoyl-sn-glycero-3-phophatidylcholine (POPC) [2] for two sets of parameters, covering the range of uncertainty. It is found that the head-group parameters are not critical for the result. The density profiles obtained from DPD simulations of lipid bilayers containing 200 lipid molecules are compared to previous MD simulation results [2] in Fig. 19a. The two peaks in the CH_2 density profile arise because the CH_3 chain endpoint is localised in the centre of the bilayer, and is not included in the average. In the DPD simulation the average is over all but the last c-bead, i.e. the last three carbon atoms are excluded from the average. Good correspondence with the MD simulation for either set gives confidence in the reliability of the model and parameters.

To validate the time scale a bilayer simulation is used to obtain the lateral diffusion coefficient of the lipid molecules, which can be checked against experimental and MD simulated values. For POPC the simulation result is $D_{\|} = 0.073\times10^{-5}$ cm^2/s. Some care must be taken, since the MD simulation was too short for two molecules even to swap places in the layer. Experiments [69,70] indicate lateral diffusion coefficient of DOPC to be in the range $D_{\|} = 0.036\times10^{-5}$ cm^2/s and $D_{\|} = 0.02\times10^{-5}$ cm^2/s. In the DPD simulation the mean square displacements parallel (and also perpendicular) to the bilayer were averaged. During this run each lipid molecule travelled 10 times the nearest neighbour distance on average. The diffusion coefficient in the DPD simulation is $D_{\|} = 0.06\times10^{-5}$ cm^2/s. This lateral diffusion coefficient compares well with the experimental ($0.02-0.04\times10^{-5}$ cm^2/s) and MD simulation (0.07×10^{-5} cm^2/s) values in the literature, even though no attempt has been made to match the relative viscosity of the lipid phase.

To investigate the structure of mixtures of lipid/surfactant bilayers, a series of simulations was done with 540 membrane molecules, surfactant or lipid, at a surfactant mole-fraction varying from 10 % to 100 % in steps of 10 %. Simulations have been done both with $C_{12}E_6$ (bead structure c_4e_4) and with C_9E_8 (bead structure c_3e_5). First we concentrate on the results regarding $C_{12}E_6$. The system with 90 % mole-fraction $C_{12}E_6$ displays holes that move around. They are relatively stable, the typical life-time is 20 –

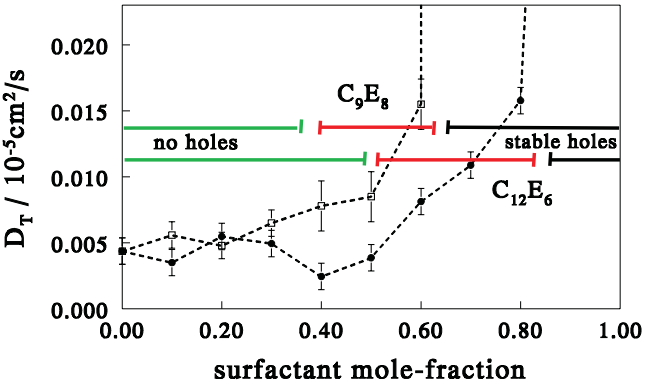

Fig. 20. Transverse water diffusion coefficient of water through the bilayer in the presence of surfactant, after [13]

40 ns, and over the course of the run there is hardly ever a conformation without a hole in the patch of $124\,\mathrm{nm}^2$. Systems with mole-fraction 80 % or less of surfactant do not show stable perforated conformations. Occasionally small holes do appear, but they disappear very quickly. At 80 % mole-fraction surfactant the typical life-time of a hole is some 0.4 – 1 ns.

The diffusion of water perpendicular to the layers provides a useful way of testing the porosity of the bilayers. To interpret these results, we first solve the diffusion equation for the mean square displacement of water in a narrow slit of impenetrable walls at distance L. For diffusion coefficient D, the mean square displacement perpendicular to the walls follows analytically as

$$\frac{R_\mathrm{s}^2(t)}{L^2} = \frac{1}{6} - \frac{16}{\pi^4} \sum_{n\ \mathrm{odd}} n^{-4} \exp\left(-\frac{n^2\pi^2 Dt}{L^2}\right) \approx \frac{1}{6}\left[1 - \frac{96}{\pi^4}\mathrm{e}^{-t/\tau} - \left(1 - \frac{96}{\pi^4}\right)\mathrm{e}^{-9t/\tau}\right]. \quad (6)$$

The first expression is exact. The second is a good approximation that can be used for curve fitting. To find a reliable value for the transverse diffusion coefficient, the mean square displacement of water normal to the bilayers is recorded, and the transverse diffusion is obtained by fitting the data to

$$R^2(t) = aR_\mathrm{s}^2(t;\tau) + 2D_\perp t,$$

where R_s^2 is the diffusion in a slit given by (6), and a and τ are free fit parameters. The resulting transverse diffusion of water is shown in Fig. 20 as a function of the surfactant mole-fraction in the layer.

It is found that up to, and including, mole-fraction of 50 % $C_{12}E_6$, the diffusion of water through the bilayer is independent of the amount of added surfactant. From that point onwards the water diffusion through the layers steadily increases. This increase is attributed to the formation of small holes that open and close on a time-scale of 0.5 ns or less, depending on the surfactant content. Permanent holes occur at 90 % surfactant. Consequently the transverse diffusion coefficient increases sharply above 80 % surfactant.

The transverse diffusion of water through the PE/C_9E_8 bilayer is also shown in Fig. 20. We see the same qualitative picture involving the creation and annihilation of small transient holes, followed by a phase with stable holes at higher surfactant content. However, the range of surfactant concentrations over which transient holes occur is much shorter than for $C_{12}E_6$. Also, the point where stable holes are formed is reached already at 70 % mole-fraction of surfactant. The real transition points must be between 60 and 70 % for C_9E_8 and between 80 and 90 % for $C_{12}E_6$, i.e. some 56 % and 78 % by weight respectively. The approximate ranges where no holes, fluctuating holes and stable holes occur are indicated in Fig. 20 by bars.

4.3 Biomembrane Deformation and Rupture

So far we have been concerned only with membranes at vanishing surface tension. However, in many cases it is found that dividing cells are particularly vulnerable. Dividing cells are not necessarily in a state of vanishing membrane tension. For instance, when yeast cells divide, their cell membrane buds out of the cell wall and is no longer protected by it. Instead the membrane is exposed to the solution. The osmotic pressure difference between inside and outside of the cell then leads to a finite surface tension on the membrane. The membrane will react to this osmotic pressure by expanding, which is an obvious prerequisite for cell division when the budding mechanism is pertinent. If the membrane cannot withstand this expansion, the cell will die. For these reasons it is prudent to simulate cell membranes under strain, rather than to study them at zero surface tension, as far as the mechanism for cell-death is concerned. Simulations of mixed membranes of lipid and $C_{12}E_6$ were undertaken in which the membrane is stretched over time, leading to increasing tension and ultimately to rupture. An example of this process is shown in Fig. 21, where the actual creation and expansion of holes is monitored. The successive frames are taken at time intervals of 1.2 ns and the patches are $17\times17\,\mathrm{nm}^2$ across. This membrane consists of 70 % PE and 30 % $C_{12}E_6$. It ruptures when its area is increased by 74 %.

The full stress history of the expanding membrane is followed in simulation. Each system is left to equilibrate over 5.3 ns after which time the y- and z-coordinates are expanded by a factor 1.03, while the x-coordinates are contracted by a factor 0.94. This cycle is repeated 12 times. This gives the yield curves shown in Fig. 22 for 10, 50 and 80 % mole fraction surfactant. Each simulation shows a clear rise in surface tension, up to a critical point where the layer fails. These simulations predict that adding surfactant to a lipid membrane significantly reduces the strength and maximum stretch of the membrane. This holds even at amounts of surfactant that have no measurable influence on the level of water diffusion through a stress-free bilayer. Without surfactant the membrane area may be increased by 100 % before it ruptures, but at a 50 % mole-fraction of surfactant this tolerance is reduced to a mere 50 % area increase. Also the maximum tension that the membrane can take reduces from 67 mN / m at 0 % surfactant, to 41 mN / m at 50 % surfactant.

The trends predicted imply that the cell will become more sensitive to the osmotic pressure difference between inside and outside, when it is exposed to a surfactant solution. For a bilayer containing 50 % mole-fraction surfactant, the pressure tolerance is reduced by some 40 %. This will have dramatic influence on the survival chances of

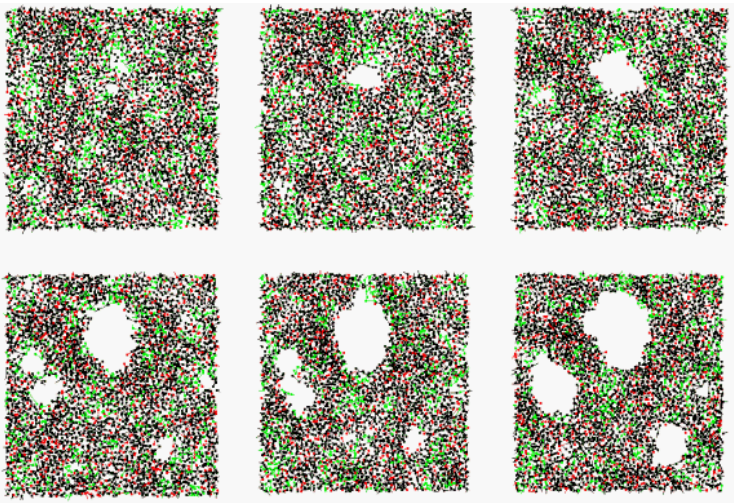

Fig. 21. Rupture process of a simulated biomembrane, after [13]

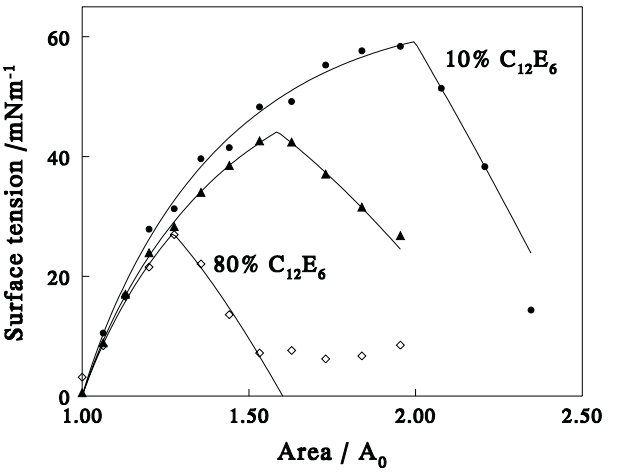

Fig. 22. Stress-strain curves for biomembranes at various amounts of surfactant, after [13]

dividing cells. Another system for which these simulations are relevant is red blood cells. These cells do not have a cell wall, but only a cell membrane. Therefore the membrane is directly exposed to the solution, and has to accommodate for all osmotic pressure differences. When the maximum pressure that a cell can withstand by incorporation of surfactant decreases below the actual osmotic pressure, the membrane ruptures. These simulations give a possible explanation why red blood cells lyse when they are exposed to a surfactant solution.

5 Conclusions

In summary, dissipative particle dynamics is a flexible method and easy to code simulation method. It has already been applied successfully to a wide variety of problems, even though we deal with a relatively new technique. The strong points of the method are: it is very competitive for hydrodynamics of polymers and mesophases, useful for multiphase flows, porous media, colloidal dispersions, etc. It is able to produce molecularly detailed simulations up to microseconds. In this mode it is faster than full atomistic Molecular Dynamics by many orders of magnitude.

The down sides of the method are the following: diffusion is too fast, the speed of sound is too low, the equation of state not always realistic, and parameterisation is a problem for detailed chemistry. With respect to these points it should be mentioned that the first is not always a problem, but actually contributes to the speed of evolution. For multiphase flow where both diffusive and hydrodynamic processes are important, this flaw can be repaired using the Andersen Monte Carlo method for the velocity randomisation [23]. Also the equation of state can be made more realistic if required [19]. Finally, the parameterisation problem for molecular simulation is a general problem in mesoscopic simulation, and not specific to dissipative particle dynamics.

Acknowledgements

S. Jury, P. Bladon, M. Cates, S. Krishna, M. Hagen, N. Ruddock, P. Warren, N. Spenley, C. Wijmans, B. Smit, T. Madden, D.J. Tildesley, and K. Rabone are kindly acknowledged for permission to reproduce their work.

References

1. D.B. Tieleman, S.J. Marrink, H.J.C. Berendsen: BBA-Rev. Biomembr. **1331**, 235 (1997)
2. H. Heller, M. Schaefer, K. Schulten: J. Phys. Chem. **97**, 8343 (1993)
3. R. Lipowsky, S. Grotehans: Europhys. Lett. **23**, 599 (1993)
4. E. Lindahl, O. Edholm: Biophys. J. **79**, 426 (2000)
5. R.D. Groot, P.B. Warren: J. Chem. Phys. **107**, 4423 (1997)
6. P.J. Hoogerbrugge, J.M.V.A. Koelman: Europhys. Lett. **19**, 155 (1992)
7. P. Espanol: Phys. Rev. E **52**, 1734 (1995)
8. P. Espanol, P. Warren: Europhys. Lett. **30**, 191 (1995)
9. I. Vattulainen, M. Karttunen, G. Besold, J.M. Polson: J. Chem. Phys. **116**, 3967, (2002)
10. M.P. Allen, D.J. Tildesley: *Computer Simulation of Liquids* (Clarendon, Oxford 1987)
11. W.K. Den Otter, J.H.R. Clarke: Int. J. mod. Phys. C **11**, 1179 (2000)
12. I. Pagonabarraga, M.H.J. Hagen, D. Frenkel: Europhys. Lett. **42**, 377 (1998)
13. R.D. Groot, K.L. Rabone: Biophys. J. **81**, 725 (2001)
14. J.R. Partington, R.F. Hudson, K.W. Bagnall: Nature **169**, 583 (1952)
15. C.M. Wijmans, B. Smit, R.D. Groot: J. Chem. Phys. **114**, 7644 (2001)
16. P. Espanol: Europhys. Lett. **40**, 631 (1997)
17. J.B. Avalos, A.D. Mackie: Europhys. Lett. **40**, 141 (1997)
18. P. Espanol: Phys. Rev. E **57**, 2930 (1998)
19. I. Pagonabarraga, D. Frenkel: J. Chem. Phys. **115**, 5015 (2001)

20. X.F. Yuan, R.C. Ball, S.F. Edwards: J. Non-Newtonian Fluid Mech. **46**, 331 (1993)
21. J.J. Monaghan: Annu. Rev. Astron. Astr. **30**, 543 (1992)
22. C.P. Lowe, M.W. Dreischor: Simulating the Dynamics of Mesoscopic Systems, Lect. Notes Phys. **640**, 35 (2004)
23. C.P. Lowe: Europhys. Lett. **47**, 145 (1999)
24. A.K. Gunstensen, D.H. Rothman, S. Zaleski, G. Zanetti: Phys. Rev. A **43**, 4320 (1991)
25. J.G.E.M. Fraaije, B.A.C. van Vlimmeren, N.M. Maurits, M. Postma, O.A. Evers, C. Hoffmann, P. Altevogt, G. Goldbeck-Wood: J. Chem. Phys. **106**, 4260 (1997)
26. E.S. Boek, P.V. Coveney, H.N.W. Lekkerkerker, P. van der Schoot: Phys. Rev. E **55**, 3124 (1997)
27. A.T. Clark, M. Lal, J.N. Ruddock, P.B. Warren: Langmuir **16**, 6342 (2000)
28. K.E. Novik, P.V. Coveney: Phys. Rev. E **61**, 435 (2000)
29. P.B. Warren: Phys. Rev. Lett. **8722**, 5702 (2001)
30. M.E. Cates, V.M. Kendon, P. Bladon, J-C. Desplat: Faraday Discuss. **112**, 1 (1999)
31. F.S. Bates, G.H. Fredrickson: Annu. Rev. Phys. Chem.**41**, 525 (1990)
32. L. Leibler: Macromolecules **13**, 1602 (1980)
33. M. Doi, S.F. Edwards: *The Theory of Polymer Dynamics* (Clarendon, Oxford 1986)
34. N.A. Spenley: Europhys. Lett. **49**, 534 (2000)
35. F.S. Rowlinson, B. Widom: *Molecular Theory of Capillarity* (Clarendon, Oxford 1982)
36. R.D. Groot, T.J. Madden: J. Chem. Phys. **108**, 8713 (1998)
37. M.W. Matsen, F.S. Bates: Macromolecules **29**, 1091 (1996)
38. R.D. Groot, T.J. Madden, D.J. Tildesley: J. Chem. Phys. **110**, 9739 (1999)
39. J. Zhao, B. Majumdar, M.F. Schulz, F.S. Bates, K. Almdal, K. Mortensen, D.A. Hajduk, S.M. Gruner: Macromolecules **29**, 1204 (1996)
40. I.W. Hamley, K.A. Koppi, J.H. Rosedale, F.S. Bates, K. Almdal, K. Mortensen: Macromolecules **26**, 5959 (1993)
41. G.H. Fredrickson, E. Helfand: J. Chem. Phys. **87**, 697 (1987)
42. R.G. Larson: J. Chem. Phys. **96**, 7904 (1992)
43. M. Schwab, B. Stühn: Colloid and Polym. Sci. **275**, 341 (1997)
44. R.D. Groot, T.J. Madden. In: *Structure and Dynamics in the Mesoscopic Domain*, ed. by Kulkami, Lal (Imperial College Press, London 1998), p. 288
45. N.P. Balsara, B.A. Garetz, M.C. Newstein, B.J. Bauer, T.J. Prosa: Macromolecules **31**, 7668 (1998)
46. M.W. Matsen: Phys. Rev. Lett. **80**, 4470 (1998)
47. R.G. Larson: Personal Communication, (1998)
48. Y. Kong, C.W. Manke, W.G. Madden, A.G. Schlijper: J. Chem. Phys. **107**, 592 (1997)
49. S. Jury, P. Bladon, M. Cates, S. Krishna, M. Hagen M, N. Ruddock, P. Warren: Phys. Chem. Chem. Phys. **1**, 2051 (1999)
50. R. Nagarajan: J. Chem. Phys. **90**, 1980 (1989)
51. E. Ruckenstein, G. Huber, H. Hoffmann: Langmuir **3**, 382 (1987)
52. E.D. Goddard, K.P. Ananthapadmanabhan: *Interactions of Surfactants with Polymers and Proteins* (CRC Press, London 1993)
53. B. Cabane: J. Phys. Chem. **81**, 1639 (1977)
54. K. Chari, B. Antalek, M.Y. Lin, S.K. Sintra: J. Phys. Chem. **100**, 5294 (1994)
55. J. Vanstam, W. Brown, J. Fundin, M. Almgren, C. Lindblad: ACS Symp. Ser. **532**, 194 (1993)
56. P. M. Claesson, M. L. Fielden, A. Dedinaite, W. Brown, J Fundin: J. Phys. Chem. B **102**, 1270 (1998)
57. S. J. Mears, T. Cosgrove, T. Obey, L. Thompson, I. Howell: Langmuir **14**, 4997 (1998)
58. R.D. Groot: Langmuir **16**, 7493 (2000)
59. R.D. Groot, A. Bot, W.G.M. Agterof: J. Chem. Phys. **104**, 9202 (1996)

60. J. de Cloizeaux, G. Jannink: *Polymers in Solution, Their Modelling and Structure* (Clarendon, Oxford 1990)
61. S.L. Moore: The Mechanisms of Antibacterial Action of Some Non-Ionic Surfactants. D. Phil. Thesis, University of Brighton (1997)
62. P. Schlieper, E. Derobertis: Arch. Biochem. Biophys. **184**, 204 (1977)
63. J. Burgoyne, M.C. Holmes, G.J.T. Tiddy: J. Phys. Chem. **99**, 6054 (1995)
64. J. Gustafsson, G. Oradd, M. Almgren: Langmuir **13**, 6956 (1997)
65. J. Gustafsson, G. Oradd, M. Nyden, P. Hansson, M. Almgren: Langmuir **14**, 4987 (1998)
66. P.A. Barneveld, J.M.H.M. Scheutjens, J. Lyklema: Langmuir **8**, 3122 (1992)
67. S. Saeki, N. Kuwahara, M. Nakata, M. Kaneko: Polymer **17**, 685 (1976)
68. J.R. Lu, Z.X. Li, R.K. Thomas, E.J. Staples, I. Tucker, J. Penfold: J. Phys. Chem. **97**, 8012 (1993)
69. M.H. Cohen, D. Turnbull: J. Phys. Chem. **31**, 1164 (1959)
70. W. Pfeiffer, T. Henkel, E. Sackmann, W. Knoll, D. Richter: Europhys. Lett. **8**, 201 (1989)